Reference: *Biol. Bull.* **231:** 26–39. (August 2016)

Using Stage- and Slit-Scanning to Improve Contrast and Optical Sectioning in Dual-View Inverted Light Sheet Microscopy (diSPIM)

ABHISHEK KUMAR[1,*], RYAN CHRISTENSEN[1], MIN GUO[1], PANOS CHANDRIS[1], WILLIAM DUNCAN[1], YICONG WU[1], ANTHONY SANTELLA[2], MARK MOYLE[3], PETER W. WINTER[1], DANIEL COLÓN-RAMOS[3], ZHIRONG BAO[2], AND HARI SHROFF[1]

[1]*Section on High Resolution Optical Imaging, National Institute of Biomedical Imaging and Bioengineering, National Institutes of Health, Bethesda, Maryland 20892-7710;* [2]*Developmental Biology Program, Sloan-Kettering Institute, New York, New York 10065; and* [3]*Program in Cellular Neuroscience, Neurodegeneration, and Repair, Department of Cell Biology, Yale University, New Haven, Connecticut 06511*

Abstract. Dual-view inverted selective plane illumination microscopy (diSPIM) enables high-speed, long-term, four-dimensional (4D) imaging with isotropic spatial resolution. It is also compatible with conventional sample mounting on glass coverslips. However, broadening of the light sheet at distances far from the beam waist and sample-induced scattering degrades diSPIM contrast and optical sectioning. We describe two simple improvements that address both issues and entail no additional hardware modifications to the base diSPIM. First, we demonstrate improved diSPIM sectioning by keeping the light sheet and detection optics stationary, and scanning the sample through the stationary light sheet (rather than scanning the broadening light sheet and detection plane through the stationary sample, as in conventional diSPIM). This stage-scanning approach allows a thinner sheet to be used when imaging laterally extended samples, such as fixed microtubules or motile mitochondria in cell monolayers, and produces finer contrast than does conventional diSPIM. We also used stage-scanning diSPIM to obtain high-quality, 4D nuclear datasets derived from an uncompressed nematode embryo, and performed lineaging analysis to track 97% of cells until twitching. Second, we describe the improvement of contrast in thick, scattering specimens by synchronizing light-sheet synthesis with the rolling, electronic shutter of our scientific complementary metal-oxide-semiconductor (sCMOS) detector. This maneuver forms a virtual confocal slit in the detection path, partially removing out-of-focus light. We demonstrate the applicability of our combined stage- and slit-scanning-methods by imaging pollen grains and nuclear and neuronal structures in live nematode embryos. All acquisition and analysis code is freely available online.

Received 19 February 2016; accepted 16 June 2016.

* To whom correspondence should be addressed. E-mail: abhishk@gmail.com

Abbreviations: CCCP, carbonyl cyanide m-chlorophenyl hydrazine; CMOS, complementary metal-oxide-semiconductor; diSPIM, dual-view, inverted, selective plane illumination microscopy; FOV: field of view; GFP, green fluorescent protein; iSPIM, inverted selective plane illumination microscopy; LSFM, light-sheet fluorescence microscopy; MEMS, micro-electro-mechanical systems; m.f.p., minutes post-fertilization; MIPAV, Medical Image Processing, Analysis, and Visualization; MTG, Mitotracker Green; PSF, point spread function; ROI, region of interest; SBR, signal-to-background ratio; sCMOS, scientific complementary metal-oxide-semiconductor; TMRE, tetramethylrhodamine ethyl ester; U2OS, human osteosarcoma cell line; 4D, four-dimensional.

Introduction

Fluorescence microscopy has proved to be a valuable tool for live-cell imaging (Fischer *et al*., 2011), due to its excellent combination of contrast and specificity. Among the many fluorescence techniques available, light sheet fluorescence microscopy (LSFM) stands out for its speed (Huisken and Stainier, 2009) and low phototoxicity (Stelzer, 2015)—advantages that directly benefit volumetric, time-lapse (4-dimensional (4D)) imaging (Winter and Shroff, 2014). By illuminating the focal plane with a thin sheet of light and synchronously sweeping the sheet and focus through the

sample, excitation is parallelized, improving speed and signal-to-noise ratio (Winter and Shroff, 2014). In LSFM, out-of-focus light is largely absent, improving contrast through "optical sectioning" and photobleaching and photodamage are confined to the vicinity of the focal plane, enabling long-term 4D imaging. Together, these features aid in the investigation of developmental biology throughout embryogenesis (Huisken *et al.*, 2004; Keller *et al.*, 2008, 2010; Wu *et al.*, 2011), brain-activity mapping in intact organisms (Ahrens *et al.*, 2013), cardiac function in model organisms (Mickoleit *et al.*, 2014), and the dynamics of protein distributions within single cells (Planchon *et al.*, 2011; Wu *et al.*, 2013).

One application of LSFM that is particularly suited to the study of single cells or small embryos (*e.g.*, those of the nematode *Caenorhabditis elegans*) is dual-view inverted selective plane illumination microscopy (diSPIM) (Wu *et al.*, 2013; Kumar *et al.*, 2014). In diSPIM, two perpendicular objective lenses alternately exchange roles in exciting and detecting fluorescence from the sample. The resulting volumes are registered and deconvolved to yield images with isotropic resolution down to ~330 nm. Moreover, diSPIM is compatible with "conventional" sample mounts such as glass coverslips. Thus, many biological samples can be prepared as they would be for wide-field or confocal imaging, and imaged easily on the diSPIM.

However, diSPIM performance—especially in laterally extended or scattering samples—can be further optimized. Because the light sheets in diSPIM are synthesized from a Gaussian beam, at distances far from the beam waist the sheet broadens and optical sectioning degrades, reducing contrast. A related problem is the lack of physical sectioning (pinholing) present in the latest diSPIM implementation. Because the entire image is collected on a wide-field area detector (camera), scattered emission light in thick, densely labeled samples can easily contaminate the desired in-focus signal. We describe simple modifications to the diSPIM that address both problems; these are based on two previous innovations (Santi *et al.,* 2009; Baumgart and Kubitscheck, 2012). First, we show that scanning the sample through a stationary light sheet allows us to use the "thin" part of the sheet (*i.e.*, near the beam waist) (Santi *et al.*, 2009), thus improving contrast in laterally extended samples such as monolayers of single cells affixed to glass coverslips. Second, we combine the slit-scanning capability of an electronic scientific complementary metal-oxide-semiconductor (sCMOS) camera with the scanning illumination used in creating the light sheet to achieve partial confocal imaging (Baumgart and Kubitscheck, 2012). Both methods improve diSPIM performance in extended, thick, or densely labeled samples, as we show by imaging a variety of fixed and live biological samples, including microtubules and mitochondria in single-cell monolayers, and nuclei and neuronal structures in nematode embryos.

Materials and Methods

Microscope

We used a previously described fiber-coupled, dual-view inverted selective plane illumination microscope (diSPIM) (Kumar *et al.*, 2014) to perform all imaging experiments. The instrument was unchanged, except that the firmware for the two scientific complementary metal-oxide-semiconductor (sCMOS) detectors was upgraded to support the recently developed "light-sheet mode" offered by the manufacturer (Hamamatsu Corporation, Bridgewater, NJ). Imaging experiments were performed while the sample was excited at wavelengths of either 488 nm, 561 nm, or both; 488-nm, long-pass, and 561-nm notch filters (cat. nos. LP02-488 and NF03-561E-25; Semrock, Inc., Rochester, NY) were used to block laser light from the detectors.

Stage-scanning

In conventional diSPIM (Kumar *et al.*, 2014), low numerical aperture (NA) illumination is introduced *via* one objective lens to create a sheet (scanned in the "y-axis" direction ("y"); Fig. 1c), and the sheet and detection focal plane are coswept through the sample (in the "z-axis" direction ("z"); Fig. 1c) to create an imaging volume (Fig. 1a). This process is repeated, switching the role of illumination and detection objective lenses. Registration and joint deconvolution are subsequently applied to fuse the two views, improving resolution isotropy (Fig. 1d). In stage-scanning mode, low NA illumination is still scanned in "y" to create a light sheet, but the sheet and detection plane are maintained at a fixed position during acquisition and the motorized sample stage is translated in the z′ direction (*i.e.*, direction in which the stage is scanned; z is the direction along which the objective lens is scanned. Hence, the z′ and z directions are at 45 degrees to each other) to obtain a volume (Fig. 1c). When acquiring volumetric data in this mode, successive imaging planes translate laterally across the field of view (FOV) (see schematic in Fig. 1c). A simple coordinate transformation converts the raw, stage-scanned data to the more familiar conventional coordinate system: the axial coordinate is scaled and the "x" lateral coordinate shifted (the other lateral coordinate, "y," is identical in both conventional and stage-scanned methods). We developed an ImageJ macro (Schneider *et al.,* 2012) that performs this shifting automatically (Guo and Shroff, 2015). After transformation *via* the macro, data are registered and deconvolved, as in conventional diSPIM, to improve resolution isotropy (Fig. 1d).

To estimate the z′ step size (*i.e.,* the distance traveled by the motorized stage between consecutive planes in stage-scan mode), we first multiplied the assumed stage-scanning speed (as specified by the manufacturer, and implemented in our acquisition code as 0.1 mm/s; Kumar and Shroff, 2015)

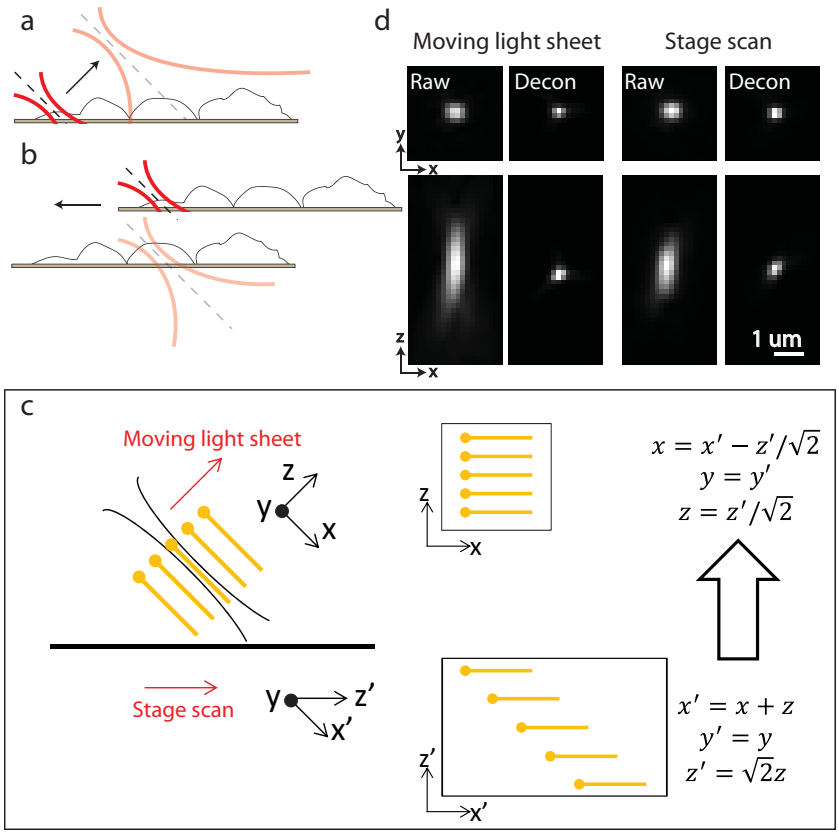

Figure 1. Concept and controls behind stage-scanning dual-view, inverted, selective plane illumination microscopy (diSPIM)**.** (a) In previous diSPIM implementation, light sheet and focal plane (dotted lines) were translated with a stationary sample. For laterally extended samples, this implied that parts of the sample, at increasing distances from the beam waist (*e.g.*, upper position of light sheet), experienced a much fatter beam, thus degrading optical sectioning and contrast. Black arrow denotes direction of the moving objective lens (as in conventional imaging) or moving stage (as in stage-scanning imaging). (b) Alternatively, if the sample is scanned by moving the stage (right to left in this diagram (black arrow)) with a stationary light sheet and focal plane, different regions in the sample consistently experience a light sheet of similar thickness. Contrast and optical sectioning are maintained by restricting the portion of the light sheet used to the optimal region of the light-sheet waist. In (a) and (b), red and pink lines define the limits of the light sheet; dashed black lines, center axis of the light sheet. (c) When acquiring a series of imaging planes (yellow lines) in stage-scanning mode, planes appear to shift laterally when viewed along the "axial" stage-scanning coordinate z′ (bottom diagram). As detailed in the diagram, a coordinate transformation is necessary to convert the raw, stage-scanned data to the "conventional" images (*i.e.*, those acquired when moving the light sheet, as shown in the upper diagram). Red lines indicate direction of motion of moving objective lens or moving stage; black lines denote the edges of the light sheet. (d) Stage-scanning (right) does not alter lateral (top row) resolution compared to conventional (left) imaging, although raw axial resolution (bottom row) is improved. This occurs in stage-scanning because a thinner portion of the light sheet is used for illumination. Joint deconvolution (Decon) improves the resolution of conventional scanning and stage-scanning to equal degrees.

by the acquisition time per plane (typically 5 ms for single-view, or 10 ms for dual-view). However, when we calculated the resulting value of z step size by following the transformation in Figure 1c, we found that the calculated value of z step size differed from the measured value of z (checked by imaging in "conventional" diSPIM) by as much as 8%. This discrepancy could be due to an accumulation of multiple errors, including light sheet tilt, collection objective lens tilt, quantization errors in the stage at low speed, or slight differences between "actual" and theoretical stage speed. To compensate for all of these potential errors, we instead measured and used an "effective" stage speed as follows: (i) First, the distance (z) between two fluorescent beads (100-nm yellow-green beads, cat. no. F-8803; Invitrogen Corp., Carlsbad, CA) was measured in "conventional" diSPIM mode, that is, by sweeping the synchronized light sheet and detection focal plane through the sample to collect an imaging volume, and using ImageJ software (Schneider *et al.,* 2012) to measure the axial distance between two beads. (ii) Next, this value was multiplied by the

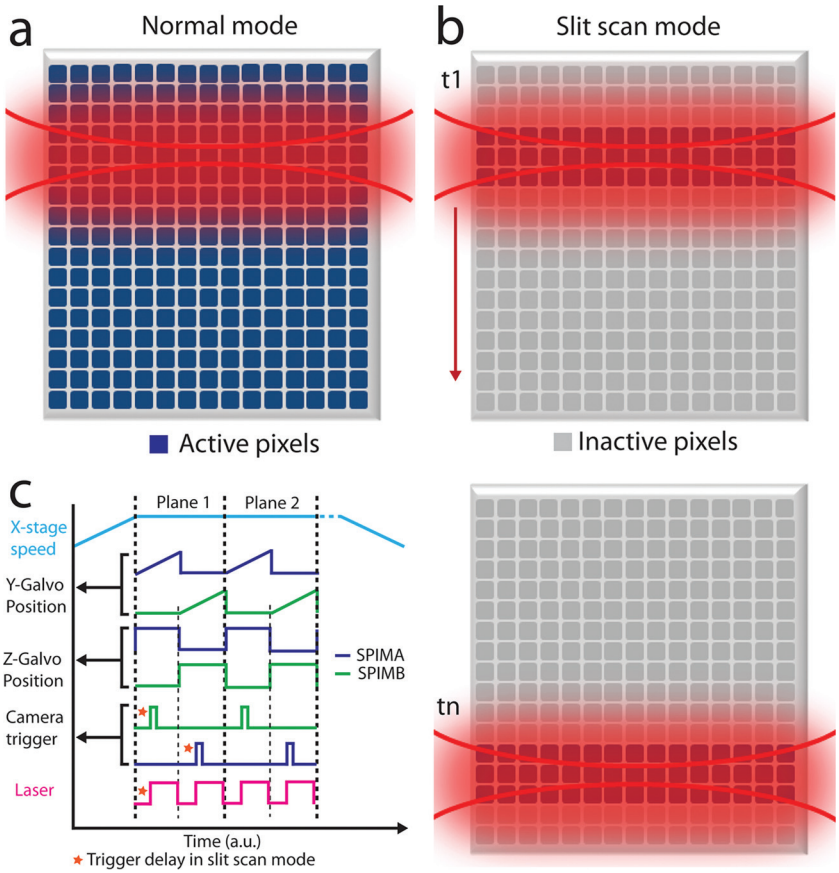

Figure 2. Illustration of the concept behind slit-scanning dual-view inverted selective plane illumination microscopy (diSPIM). (a) In conventional diSPIM, a low numerical aperture (NA) beam is swept across the sample to create a light sheet, and fluorescence is collected by exposing all pixels (blue) across the imaging field of the camera. Because all pixels are exposed, the camera records both high-quality fluorescence generated within the illumination and low-quality fluorescence scattered outside the beam (red haze outside the Gaussian beam). (b) In slit-scanning diSPIM, camera exposure is synchronized with the position of the illumination beam, exposing only a narrow band of pixels (3 pixel rows in this example) at once. Because most of the pixels are inactive (not recording light), a "virtual slit" is formed, filtering out much of the scattered haze. This virtual slit follows the position of the illumination beam, thus forming a "rolling shutter." (c) Shapes of main waveforms used in stage-scanning, slit-scanning diSPIM. The sample stage accelerates to constant velocity during acquisition. The Y-galvanometer (Y-galvo) position alternately sweeps in a sawtooth pattern, sequentially producing a sheet in selective plane illumination microscopy A (SPIMA) and B (SPIMB) views. The Z-galvo position alternately fixes and deflects the beam in each view. Finally, the camera and laser both trigger with a slight, user-defined delay, thus ensuring synchronization between rolling shutter mode, illumination, and Y-galvo position. Note that these waveforms are meant to be qualitative only; see Materials and Methods and the code for more details.

square root of 2 (Fig. 1c) to yield the corresponding z′ displacement, assuming the geometry in Figure 1c. (iii) The imaging volume was retaken in stage-scanning mode, using the assumed stage-scanning speed. The time between bead appearances was estimated by multiplying the number of apparent planes between beads by the acquisition time per plane. (iv) The z′ in (ii) was divided by the time in (iii) to yield an effective stage speed.

Since our effective stage speed was 92% of the assumed value, when transforming the data from stage-scanned to conventional view (Fig. 1c), if we desired 1-μm z step spacing between planes, we specified a z′ step size of 0.65 μm (0.92 $\times$ 0.707 μm), or 4 pixels in the "set slice step size" field, within the ImageJ shifting macro.

Figure 2c shows examples of waveforms that are input into the various diSPIM hardware components in this mode. The motorized sample stage is accelerated to constant speed (occurring over 50–100 ms), after which image acquisition commences. The light sheet is created during each exposure by applying a sawtooth wave to the y-axis of the dual-axis scan mirror within the diSPIM scan head (Y-galvanometer (Y-galvo)) waveform in Fig. 2c; Kumar *et al.*, 2014). The

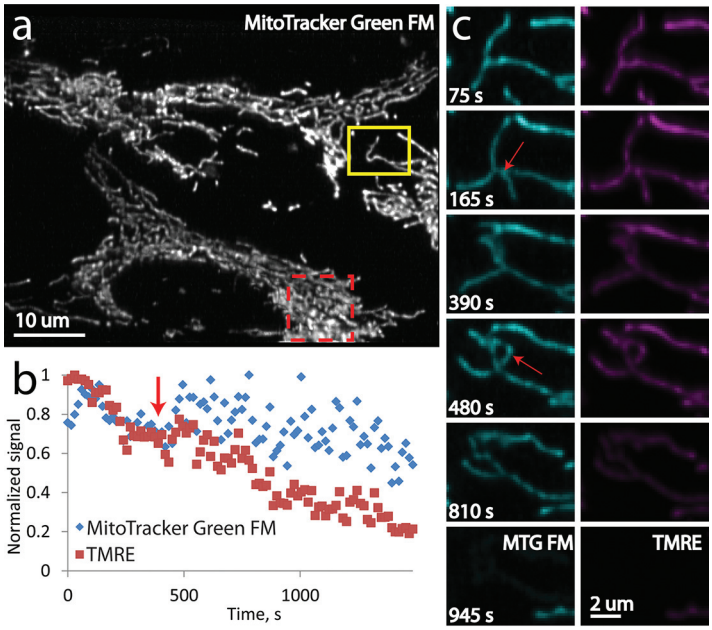

Figure 3. Stage-scanning enables interrogation of the dynamics of mitochondrial fission, fusion, and membrane potential. (a) Overview of maximum-intensity projection of the deconvolved, 4D dataset. Mitochondria in fixed human osteosarcoma (U2OS) cells were stained with MitoTracker Green FM (MTG FM; Thermo Fisher Scientific) and tetramethylrhodamine ethyl ester (TMRE), then volumetrically imaged every 15 s. For clarity, only the first time point from the MTG FM spectral channel is shown. (b) Dyes showing different rates of release from mitochondria, with MTG FM demonstrating a gradual release, and TMRE a faster exit, from the mitochondria. Plots were derived by averaging the intensity in the red-dotted square region in (a) for each spectral channel. The red arrow marks the addition of carbonyl cyanide m-chlorophenyl hydrazine (CCCP). (c) Higher-magnification views of mitochondrial dynamics in each channel, corresponding to the yellow rectangular region in (a). Fusion and remodeling events (red arrows) are visible, as is the differential leakiness of each dye (cyan, MTG FM; magenta, TMRE). See also supplementary video 3 (http://www.biolbull.org/content/supplemental).

light sheet is alternately transmitted (or deflected) to each objective lens by applying a square wave pulse to the z-axis of the dual-axis scan mirror each time an image is acquired (Z-galvanometer (Z-galvo) in Fig. 2c). Dual-view images are acquired plane-by-plane in an alternating duty cycle by applying complementary waveforms to each objective lens. For dual-color imaging (Figs. 3 and 4), two-color acquisitions are performed first for one color for both planar views, then repeated for the second color. For example, if A and B represent the two perpendicular views, and 488 nm and 561 nm are the two laser wavelengths, dual-color acquisition proceeds plane by plane as A_488, B_488, A_561, and B_561. Camera and laser triggers are synchronized with the Y- and Z-galvo waveforms, and laser and camera trigger delays (as shown by the red stars in Fig. 2c) are set to zero unless slit-scanning is desired. The LabVIEW acquisition code (National Instruments Corp., Austin, TX) and an overview of the code are available online (Kumar and Shroff, 2015).

Slit-scanning

Slit-scanning is used to partially reject out-of-focus light that originates along the ”y” direction, *i.e.*, the direction in which the illumination beam is scanned to create the sheet. In this mode, the Y-galvo scan (Y scan) is synchronized with the camera’s rolling shutter and the laser is scanned unidirectionally once for each imaging plane. The number of active pixel columns in the sCMOS detector, an adjustable parameter, allows the user to control the width of the virtual slit. We found that a 20-pixel column is optimal for the light-sheet thickness we employed in these experiments. To achieve perfect synchronization between laser scan and rolling shutter of the camera, precise calibration and optimization of three parameters (in each view) were critical: Y-galvo offset (setting the starting location of the Y scan), Y-galvo amplitude (defining the extent of the Y scan), and camera trigger delay, which determines the start (timing) of the rolling shutter readout.

To set these parameters optimally, we begin by fixing the camera’s region of interest (ROI) (which, for these experiments, was 500 × 500 pixels) and determining the Y-scan offset by setting the Y-galvo amplitude to zero and examining the apparent beam position on the camera, using a fluorescent dye solution. The offset is adjusted such that the beam position with zero amplitude falls at the top edge of the camera’s ROI. To estimate the correct amplitude of the

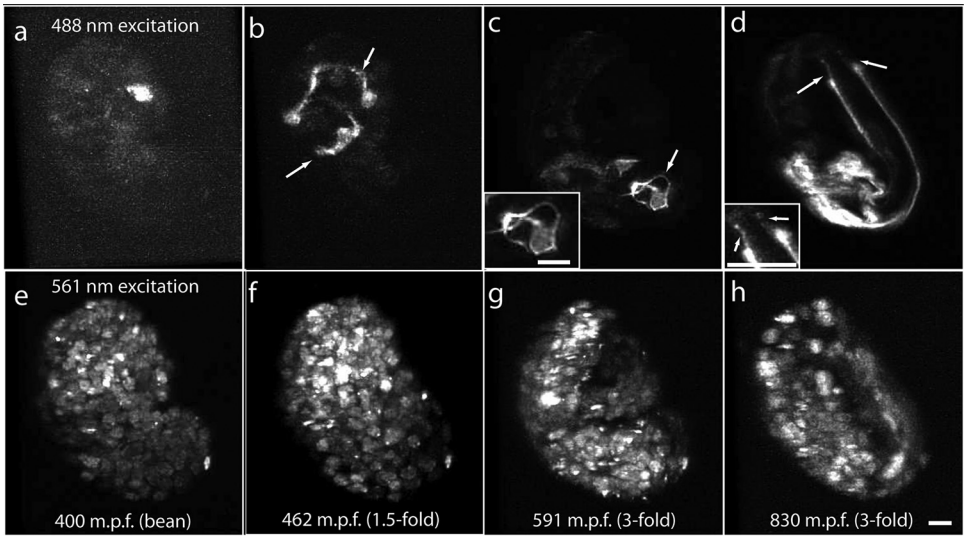

Figure 4. Dual-color imaging of developing embryos of *Caenorhabditis elegans*. (a–d) Dual-color imaging highlights the development of green fluorescent protein (GFP)-labeled neurons excited with 488 nm laser wavelengths throughout embryogenesis. (e–h) Dual-color imaging highlights corresponding mCherry-labeled histones, excited with 561 nm. Timing is in minutes post-fertilization (m.p.f.) and developmental stage of the embryo. (a) At 400 m.p.f., a single neuron is visible as the promoter begins expression. (b) Sixty-two min later, expression in additional neurons is visible. Arrows indicate developing neurites. (c) The embryo at 591 m.p.f. The outgrowth of neurites is almost complete. (d) Expression in amphid neurites is now visible. Arrows point to ciliated dendrite ending for one pair of amphid neurites. Insets in (c, d) provide a higher-magnification view of the neurites and ciliated tip. (e) mCherry image of the embryo, corresponding to (a). Note the clearly visible nuclei. (f) This image corresponds to the image in (b). Note the beginning of elongation. (g) This image corresponds to (c). Elongation continues; the embryo is now in the early three-fold stage. (h) This image corresponds to (d)**.** Elongation is complete. All scale bars = 5 μm. Maximum-intensity projections are shown.

Y-galvo, the beam is positioned at the other edge of the camera by appropriately changing the Y-galvo offset. The difference in Y-galvo offset values provides a good starting guess for the Y-galvo amplitude. Next, we set the camera trigger by providing a delay to the camera trigger signal (Fig. 2c) with respect to the Y-galvo sweep. For the settings in this study, we set the delay to ~2.5 ms. We also iterated the camera trigger delay around that value in small steps (~100 μs) to obtain the optimum delay. ("Optimum" is visually obvious: the camera's ROI is "painted" only when the slit and shutter are well synchronized. See online tutorial (Kumar and Shroff, 2015)). Once the trigger delay is optimized, we then reiterate over the Y-galvo amplitude (in 0.01-mV steps) for best synchronization. Once these parameters are optimized, they are considered fixed for the given ROI and not changed. We note that in the Orca Flash 4.0 V2 Camera (Hamamatsu Photonics), slit width is defined by the ratio of the line exposure to the line readout time (the readout time can be set in multiples of ~10 μs). For our experiments, we fixed the line readout time at 10 μs and changed the line exposure time. The effective acquisition time per plane in slit-scanning is thus the sum of the readout time for the ROI (500 pixels × 10 μs/pixel = 5 ms), camera trigger delay (~2.5 ms), and line exposure time (200 μs), or ~8 ms. The LabVIEW acquisition code and an overview of the code are described online (Kumar *et al.*, 2015).

Sample preparation

Microtubules in cultured U2OS human osteosarcoma cells (HTB-96; ATCC ("American Type Culture Collection"), Manassas, VA) were immunolabeled as follows: Cells were grown on #1.5, 24 × 50-mm coverslips suitable for diSPIM; washed 3 times in cytoskeletal buffer (CB; 10 mmol l^{-1} PIPES, 138 mmol l^{-1} KCl, 3 mmol l^{-1} 3×$MgCl_2$, 2 mmol l^{-1} EGTA, 0.01% NaN_3, 160 mmol l^{-1} sucrose, pH 6.8); precleared in cold CB containing 0.2% Triton X-100 (vol/vol) for 30 seconds; fixed and permeabilized for 30 min at 37 °C in a mixture of 0.5% glutaraldehyde, 3.7% formaldehyde, and 0.3% Triton X-100 (vol/vol) in CB; washed 5 times with CB, and quenched 3 times in ice-cold CB containing 100 mmol l^{-1} glycine. Cells were washed one time with CB between each round of quenching. After quenching, cells were washed 3 times with CB and blocked in antibody dilution buffer (AbDil; 150 mmol l^{-1} NaCl, 20 mmol l^{-1} Tris, 0.1% Triton X-100 (vol/vol), 0.1% NaN_3, 4% BSA, pH 7.4) for 1 h, and rocked gently on an agitator

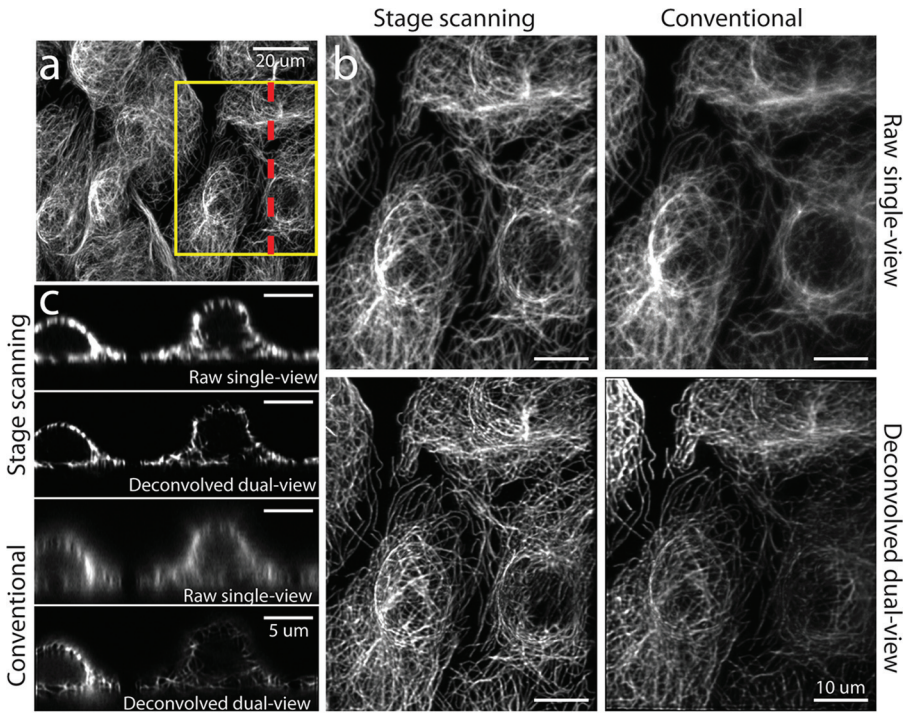

Figure 5. Stage-scanning improves the performance of dual-view inverted selective plane illumination microscopy (diSPIM) across large fields of view. (a) Raw, single-view, stage-scanned image over a 86 × 101-μm field of view. Image is a lateral, XY, maximum-intensity projection of Alexa-Fluor (AF-488)-immunolabeled microtubules in fixed human osteosarcoma (U2OS) cells. Note the consistent image quality across the entire field of view. (b) Comparative, higher-magnification views of the area in the yellow rectangle in (a). Note the degradation in contrast toward the right side of the imaging field, due to increased light-sheet thickness. (c) Axial YZ slice along the dotted line in (a). Conventional diSPIM imaging has additional haze, which is still present after deconvolution. The stage-scanned images (raw, single-view and deconvolved, dual-view) are free of haze. See also supplementary videos 1 and 2 (http://www.biolbull.org/content/supplemental).

(Lab Quake; Thermo Fisher Scientific, Waltham, MA). After blocking, AbDil was aspirated and cells were incubated with 4 μg/ml monoclonal mouse anti-α-tubulin primary antibody (product no. T6199; Sigma-Aldrich, St. Louis, MO) in AbDil for 2 h at room temperature with rocking, washed 5 times in Abdil, incubated in a 1:200 dilution of Alexa fluor 488 Goat antimouse secondary antibody (product no. A11001; Molecular Probes Co., Eugene, OR) in AbDil for 3 h at room temperature with rocking, washed 4 times with AbDil, washed 4 times in deionized water, and imaged (Fig. 5).

We performed live mitochondrial imaging in the U2OS cell line (Fig. 3). The cells were maintained in Dulbecco's Modified Eagle's culture medium (DMEM; Sigma-Aldrich) supplemented with glucose 1 g l^{-1}, glutamine 1 mmol l^{-1}, pyruvate 1 mmol l^{-1}, and 10% fetal bovine serum (FBS; Hyclone), and grown in a 5% CO_2 environment at 37 °C. Two days before imaging, the cells were plated onto #1.5, 24 mm × 50 mm rectangular coverslips that had been acid-treated in 1 mol l^{-1} HCl overnight, rinsed extensively with deonized water, submerged in boiling Milli-Q water (Millipore Corp., Billerica, MA) for 5 min, rinsed again with cold Milli-Q water, and autoclaved. During imaging, we used low-glucose (1 g l^{-1},) DMEM supplemented with glutamine, pyruvate, and 10% FBS without phenol red and antibiotics. To characterize mitochondrial dynamics and to observe changes in membrane potential, we labeled the cells with 25 nmol l^{-1} tetramethylrhodamine ethyl ester (TMRE; Sigma-Aldrich), which accumulates in mitochondria as a function of mitochondrial membrane potential. They were also labeled with 200 nmol l^{-1} of MitoTracker Green FM (Fei Mao, dye developer; MTG FM; Thermo Fisher Scientific), which preferentially binds to thiol groups on mitochondrial proteins. To generate uncoupling of oxidation from phosphorylation and energy production, followed by membrane potential collapse, we added carbonyl cyanide m-chlorophenyl hydrazine (CCCP; product no. C2759; Sigma-Aldrich) to a final concentration of 1 μmol l^{-1} 6 min to the experiment.

Ragweed pollen grains (cat. no. 07673-1; Polysciences, Warrington, PA; Fig. 6) were spread over Poly-l-lysine-coated coverslips, washed gently with water to remove unstuck pollen, and imaged.

For lineaging a stage-scanned embryonic dataset (Fig. 7),

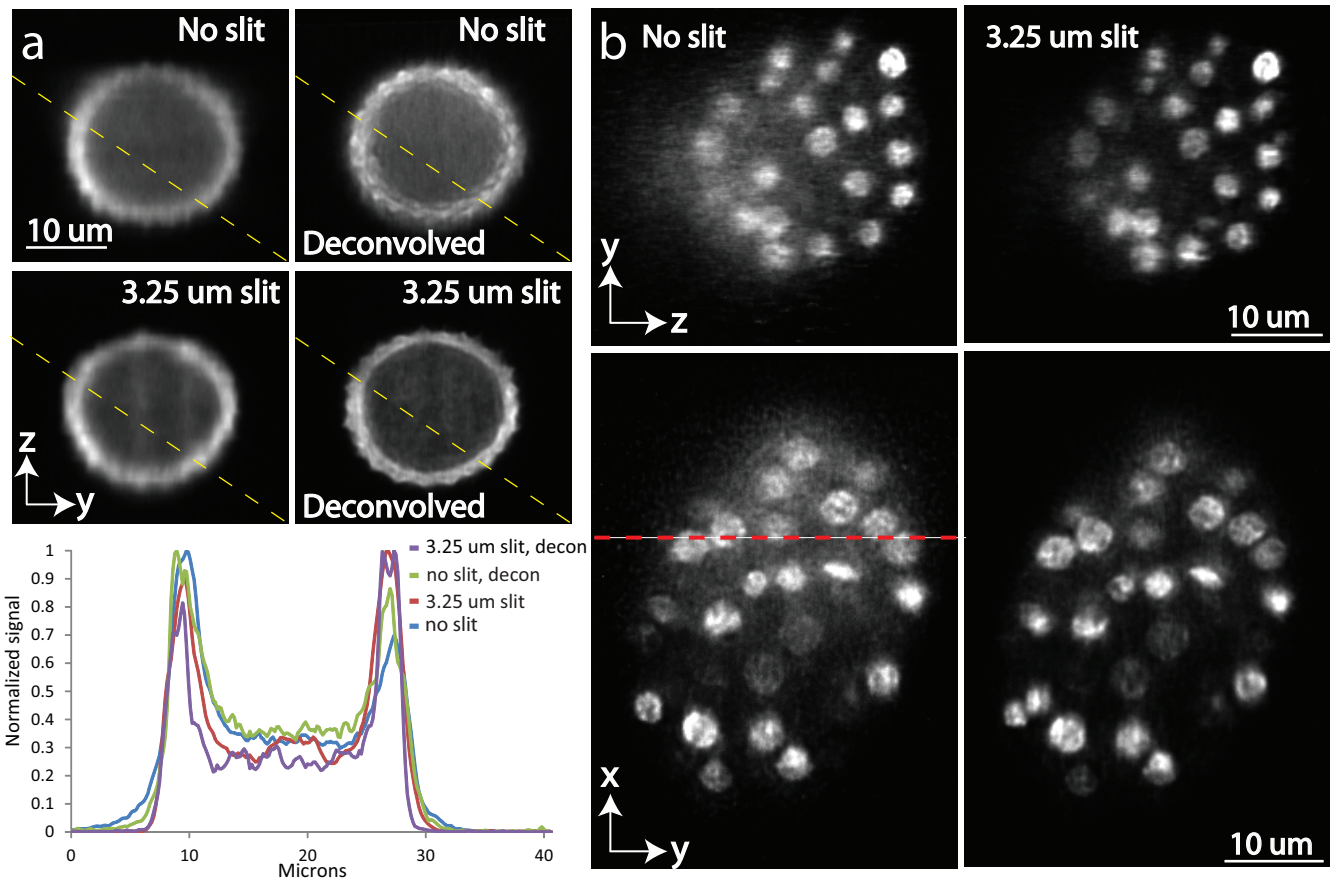

Figure 6. Slit-scanning further improves contrast and optical sectioning of dual-view inverted selective plane illumination microscopy (diSPIM). (a) Comparative imaging of ragweed pollen (*i.e.*, single axial slices through a pollen grain) without (top row) and with (middle row) a 3.25-μm rolling slit. Scattered fluorescence external to and within the pollen grain is reduced after slit-scanning in both raw (left column) and deconvolved (right) images. The graph at the bottom shows line profiles corresponding to the yellow dashed lines in imaging, confirming that deconvolved (decon), slit-scanned images show superior contrast and sectioning. (b) Comparative imaging without (left column) and with (right column) slit-scanning, highlighting single slices axially (top row) and laterally (bottom row) through a live, green fluorescent protein-histone (GFP-histone)-labeled worm embryo. The axial slices correspond to the red dashed line in the lateral slices. As in (a), the slit-scanned images show an obvious reduction in scattered haze, enabling clearer observation of individual nuclei. All images in (b) have been deconvolved; all images in (a) and (b) are derived from stage-scanned datasets; and "y" corresponds to the direction of the slit-scanning. See also supplementary video 5 (http://www.biolbull.org/content/supplemental).

Caenorhabditis elegans embryos derived from strain BV276 ujIs113 (pie-1::mCherry::H2B + unc-119(+); pnhr-2::mCherry::histone + unc-119(+)) II were used. *C. elegans* embryos derived from strain BV24 were used for green fluorescent protein (GFP)-histone experiments in Figure 6. For dual-color experiments in Figure 4, we imaged worms belonging to the strain SLS-2 olaex2537 ((pncs-1::GFP; punc-122:mCH); ujIs113 (pie-1::mCherry::H2B + unc-119(+); pnhr-2::mCherry::histone + unc-119(+)) II). The SLS-2 strain was created by crossing together animals belonging to strains DCR 4315 olaex2537 (pncs-1::GFP; punc-122:mCH) and BV276 ujIs113 (pie-1::mCherry::H2B + unc-119(+); pnhr-2::mCherry::histone + unc-119(+) II). All nematode embryos were prepared and imaged in diSPIM, as previously described (Kumar *et al.*, 2014).

Lineaging

After imaging, data were shifted, cropped, and background-subtracted using the stage-scanning ImageJ macro. After shifting and cropping, embryo volumes were rotated in ImageJ so that the anterior end of the embryo was on the left side of the volume. Rotated images were registered and deconvolved using the GenerateFusion plugin in Medical Image Processing, Analysis, and Visualization (MIPAV) (McAuliffe *et al.*, 2001). After deconvolution, volumes

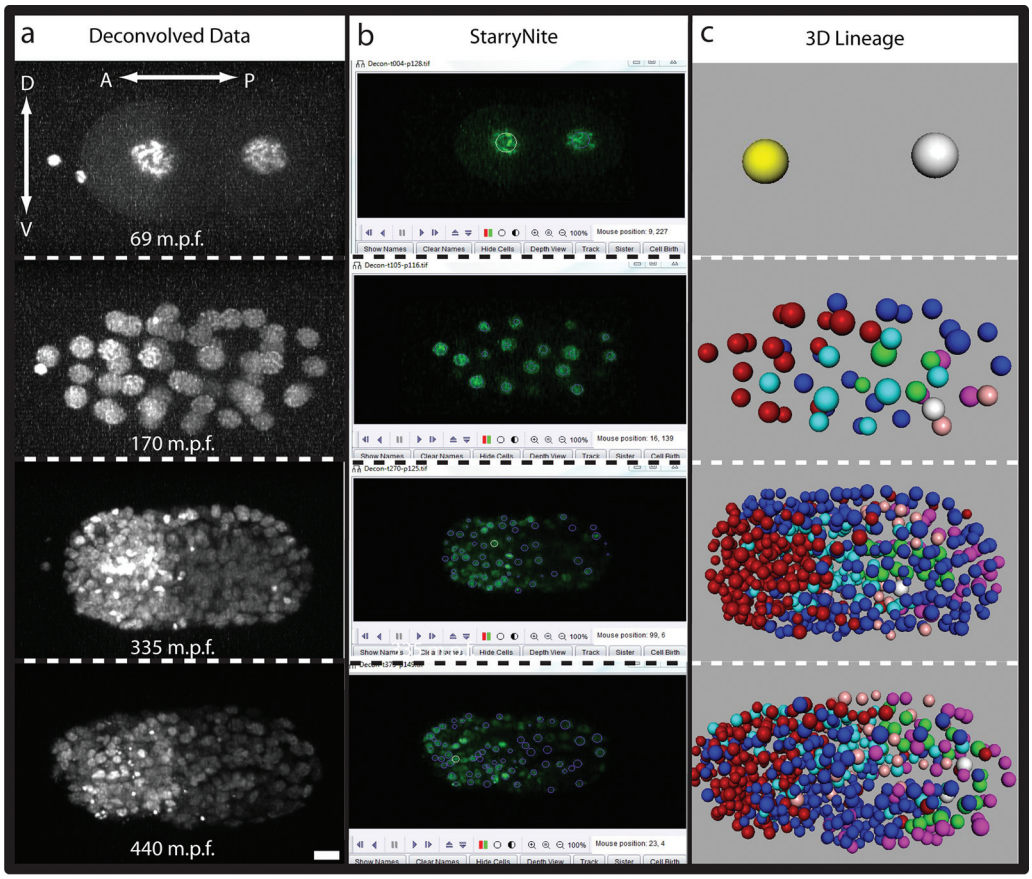

Figure 7. Lineaging a nematode embryo using stage-scanning dual-view inverted selective plane illumination microscopy (diSPIM). (a) Deconvolved diSPIM maximum-intensity projections at indicated minutes post-fertilization (m.p.f.). In this dataset, twitching begins at 444 m.p.f. Arrows show direction in the embryo: D, dorsal; V, ventral; A, anterior; P, posterior. Scale bar = 5 μm. (b) Representative single planes as viewed in StarryNite ver. III lineaging software (Bao *et al.,* 2006), corresponding to the time points shown in (a). Green spots in the slices represent nuclei in the diSPIM image volumes; purple circles around the nuclei are cell identities assigned and tracked by StarryNite. (c) Renderings showing all nuclei tracked by StarryNite at the time points shown in (a). Different sublineages are represented by different colors. Top panel: yellow, AB; white, P1. All other panels: red, ABa; blue, ABp; magenta, C; pink, D; green, E; cyan, MS; white, P4. 3D lineage, 3-dimensional positions of lineaged cells. See also supplementary video 4 (http://www.biolbull.org/content/supplemental).

were run through StarryNite ver. III (July 2014 build; Bao *et al.,* 2006) to identify nuclei. AceTree (Bao *et al.*, 2006) was used to manually edit the StarryNite III results to generate the lineage projections in Figure 7c.

Imaging parameters

Spacing between planes was set at 0.5 μm for all conventional diSPIM imaging, and 0.65 μm (after shifting, *i.e.*, the z, not z′ parameter described in Fig. 1c). For bead imaging (Fig. 1d), 100 planes/volume/view were acquired in conventional mode, and 75 planes/volume/view were acquired in stage-scanning mode, at 5 ms/plane. For microtubule imaging (Fig. 5), 200 planes/volume/view were acquired in conventional mode and 160 planes/volume were acquired in stage-scanning mode at 5 ms/plane. Stage-scanning, dual-color imaging of mitochondria (Fig. 3) was performed at 75 planes/volume/view/color at 5 ms/plane/color; a 15-s pause was introduced between imaging volumes. Single-color nematode imaging for lineaging (Fig. 7) was performed at 5 ms/plane and at 100 planes/volume/view. A 60-s pause was introduced between imaging volumes and focus was checked manually every hour, adjusting as necessary to control for focus drift. For pollen grain imaging (Fig. 6a), 50 planes/volume/view were acquired at 5 ms/plane in conventional mode and 8 ms/plane were acquired in slit-scanning mode. For strain BV24 embryo imaging (Fig. 6b), 60 planes/volume/view were acquired at 5 ms/plane in conventional mode, and 8 ms/plane were acquired in

slit-scanning mode. For dual-color, stage-, and slit-scanning embryonic imaging (Fig. 4), 70 planes/volume/color were acquired at 8 ms/plane; a 60-s pause was introduced between consecutive, dual-color volumes.

Deconvolution

Cropping, background subtraction, registration, and joint deconvolution were performed using the MIPAV environment, as previously described (Kumar *et al.*, 2014). We used the following full-width, half-maximum parameters when performing deconvolution: View A, 3.3, 3.0, and 9.5 pixels; and View B, 9.5, 3.0, and 3.2 pixels. An updated guide to using deconvolution in MIPAV is described online (Christensen *et al.,* 2015).

Signal-to-background ratio comparisons

To estimate the signal-to-background ratio (SBR) in Figure 5, we computed the ratio of the mean intensity of a 20 $\times$ 20-pixel region within the sample ("signal") to the mean intensity of a region of identical size outside the sample ("background"). Because local signal and background vary across the sample, this estimate was computed at three different locations for the dataset presented in Figure 5b. To estimate SBR in Figure 6b, we computed the ratio of the mean intensity of a nuclear region ($\sim$20-pixel diameter) to the mean intensity of a non-nuclear region of identical size for 5 different nuclei. To report the improvements in SBR as reported in the text, we computed the ratio of each SBR measurement in stage-scanning *versus* conventional-scanning mode (for data in Fig. 5) and slit-scanning *versus* conventional mode (for data presented in Fig. 6).

Results

In conventional dual-view inverted selective plane illumination microscopy (diSPIM), a high-speed, micro-electro-mechanical system (MEMS) mirror moves the excitation sheet through a sample, while a piezoelectric collar synchronously moves the detection objective lens to keep the focal plane coincident with the illuminated plane (Kumar *et al.*, 2014) (Fig. 1a). While this technique works well for small, cell-sized samples, it is less effective for larger, extended samples, because the thickness of the light sheet eventually broadens to the extent that most of the sample (outside the focal plane) is illuminated (Fig. 1a). This illumination of out-of-focus areas lessens the effectiveness of light sheet fluorescence microscopy (LSFM) by contaminating images with extraneous light and introducing phototoxicity (without compensating benefits) in the out-of-focus areas. We reasoned that, for many samples, translating the sample laterally through a fixed light sheet and focal plane would enable imaging with an effectively thinner sheet, because only the region of excitation near the beam waist would be used to illuminate the sample (Fig. 1b, c; see also Materials and Methods above).

We implemented this "stage-scanning" mode simply by translating the motorized specimen stage unidirectionally at constant velocity, while keeping light sheet and detection optics stationary. As long as the stage velocity is set to less than the point-spread function (PSF) width/exposure time (in this case, 500 nm/5 ms, or $\sim$0.1 mm s^{-1}), the effects of motion blur are negligible and spatial resolution is equivalent to the more conventional imaging mode, in which detection objective lens and light sheet are translated together. We characterized spatial resolution by imaging 100-nm, yellow-green fluorescent beads, comparing their apparent size in both stage-scanning and conventional modes (Fig. 1d). Lateral resolution was equivalent in either mode (conventional mode full width half maximum (FWHM): x 509 $\pm$ 20 nm, y 441 $\pm$ 23 nm; stage-scan mode FWHM: x 498 $\pm$ 25 nm, y 436 $\pm$ 20 nm; $N = 10$ beads). Axial resolution in conventional mode was not uniform across the imaging field, because the light-sheet thickness varies significantly along the z′-axis (Fig. 1a, c). However, stage-scanning resulted in uniform axial resolution across the field of view (FOV), because only the beam waist was used for illumination (conventional mode: z 2112 $\pm$ 63 nm; stage-scan mode: z 1396 $\pm$ 195 nm). We observed a slight astigmatism in the PSF, likely due to an imperfection in our objective lens. As expected, joint-deconvolution (Kumar *et al.*, 2014; 20 iterations, Richardson-Lucy method) improved isotropy in all 3 spatial dimensions to $\sim$350 nm, regardless of imaging mode (Fig. 1d). We conclude that stage-scanning preserves the high spatial resolution afforded by diSPIM.

To demonstrate the ability of stage-scanning to image large fields of view (FOVs), we fixed cells that had been immunolabeled with Alexa Fluor 488, decorating microtubules, and compared the resulting images after conventional (moving light-sheet and detection objective lens) and stage-scanning diSPIM (Fig. 5). Stage-scanning enabled imaging over large FOVs ($\sim$86 $\times$ 100 μm, Fig. 5a) without loss of quality. In contrast, imaging the same field in conventional diSPIM showed pronounced degradation at the edges of the imaging field (Fig. 5b), due to the increasing thickness of the illuminating light sheet. Axial cuts through the sample (Fig. 5c) revealed prominent out-of-focus background surrounding microtubules in conventional mode (which was absent in stage-scanning mode), again due to the increased thickness of the light sheet at the edges of the field. To quantify the improvements afforded by stage-scanning, we measured the signal-to-background ratio (SBR) at three locations across the FOV. Thickness of the excitation beam increases from left to right in conventional diSPIM, but is maintained at uniform thickness in stage-scanning. This difference is reflected in the SBR, which is two to four times better in stage-scanning mode (Fig. 5b); the SBR ratio

between stage-scanning and conventional diSPIM worsens from left to right (see also Materials and Methods above). Although deconvolution sharpened microtubules and improved resolution isotropy, it could not completely remove out-of-focus background or restore image contrast (Fig. 5b, c), presumably because the low-frequency background present in conventional diSPIM images was not modeled by our PSF. We conclude that imaging over extended fields is better achieved with stage-scanning than conventional diSPIM (compare also supplementary videos 1 and 2, http://www.biolbull.org/content/supplemental).

To demonstrate the efficacy of stage-scanning diSPIM in interrogating live, two-color specimens over a large FOV, we visualized the dynamics of mitochondria in human osteosarcoma cells (U2OS) (Fig. 3a) that were labeled with MitoTracker Green FM (MTG FM; excited at 488 nm) and tetramethylrhodamine ethyl ester (TMRE; excited at 561 nm). MitoTracker Green binds to free thiol groups on cysteine residues of mitochondrial proteins, and its accumulation in mitochondria is much less dependent on mitochondrial membrane potential than TMRE, a lipophilic dye whose binding to mitochondria strictly depends on membrane potential (Presley *et al.*, 2003; Perry *et al.*, 2011). We observed transient fluctuations in intensity from both dyes. These fluctuations were more pronounced in the TMRE channel (see supplementary video 3, (http://www.biolbull.org/content/supplemental) due to mitochondrial depolarization and repolarization (Twig *et al.*, 2008). Yet transient losses in mitochondrial polarization did not hamper the ability of mitochondria to fuse (Fig. 3b). Carbonyl cyanide m-chlorophenyl hydrazine (CCCP) uncouples oxidative phosphorylation from adenosine triphosphate (ATP) production by dissipating the proton gradient, causing a decrease in mitochondrial membrane potential. We observed this effect by adding CCCP to the cells 360 s into the imaging experiment; we noted a pronounced loss in membrane potential in the TMRE spectral channel and—to a significantly lower extent—in the MTG channel (Fig. 3b, c). Imaging by diSPIM thus allows live, 4D imaging of mitochondrial dynamics, fluctuations, and gradual loss of mitochondrial membrane potential over many tens of timepoints. Stage-scanning also allowed us to interrogate these dynamics over a large field of view: mitochondria were clearly resolved throughout the $\sim$100 μm $\times$ 60-μm FOV.

The embryo of *Caenorhabditis elegans* possesses an invariant cell lineage (Sulston *et al.*, 1983), for which the fate and identity of each of the 671 embryonic cells have been mapped. Based on this lineage, semi-automated computer programs that track and identify cells in the developing nematode embryo have been created and applied to the lineaging of embryos that have been compressed between coverslip and slide (Bao *et al.*, 2006; Santella *et al.*, 2010), usually with data acquired from spinning-disk confocal microscopy. More recently, uncompressed embryos have been imaged with laser-scanning confocal or Bessel beam microscopy, and lineaged to the onset of twitching (Giurumescu *et al.*, 2012). The fast, gentle, long-term imaging capabilities of our diSPIM system also make it an attractive system for the application of lineaging software. Nevertheless, a lineage derived from diSPIM had not yet been produced by the time of our study. To generate such a lineage, we captured stage-scanning datasets of embryos expressing nuclear-localized histone::mCherry from the two-cell stage until the onset of twitching. After data processing (see Materials and Methods), we used StarryNite III and Acetree software to lineage the cells in the embryo dataset (Fig. 7). We were able to track 99% of cells in the embryo out to 365 min post-fertilization (m.p.f) and 97% of cells out to twitching (supplementary video 4, http://www.biolbull.org/content/supplemental), comparable to earlier results from other methods (Giurumescu *et al.*, 2012). Our results demonstrate the utility of the stage-scanning diSPIM system for lineaging uncompressed nematode embryos.

We have shown that stage-scanning enables high-quality imaging across fields that extend to 100 μm in either lateral direction. In contrast, in conventional diSPIM imaging is degraded over imaging fields as small as 50 μm $\times$ 50 μm (Fig. 5b). We note that, in principle, the improvements offered by stage-scanning extend to fields as large as $\sim$4 mm $\times$ 4 mm in our current sample chamber; the current limits are set by steric interference between objective lenses and the chamber walls.

Having demonstrated the capabilities of stage-scanning, we next turned our attention to a different diSPIM improvement: the introduction of partial confocal imaging (Fig. 2). Because our light sheet is constructed by scanning a low numerical aperture (NA) excitation beam in one dimension, scattered emission light (introducing unwanted background across the image; Fig. 2a) may be rejected by passing the fluorescence corresponding to our excitation through a confocal aperture before detection. This method has been used to reject background when using light sheet fluorescence microscopy (LSFM) to image whole, fixed mouse brains by de-scanning the fluorescence, filtering it through a slit, and re-scanning before collection onto a camera (Silvestri *et al.*, 2012). While effective, this method requires additional optics in the emission path, reducing collection efficiency. An elegant alternative is to employ the "rolling shutter" mode of the sCMOS detection camera, whereby columnar pixel groups are synchronized with the excitation and sequentially exposed, forming a moving "slit" that masks camera pixels outside the excitation beam (Fig. 2b; Baumgart and Kubitscheck, 2012). Inspired by the integration of this rolling shutter with other applications of LSFM (Baumgart and Kubitscheck, 2012; Chhetri *et al.*, 2015; de Medeiros *et al.*, 2015; Dean *et al.*, 2015), we added this functionality to our control code (Fig. 2c, Materials and Methods), thereby introducing partial confocality into diSPIM.

To demonstrate the improvement offered by slit-scanning, we compared images of ragweed pollen grains acquired in stage-scanning mode, both with and without a rolling slit (Fig. 6a). Although relatively small (19–20 μm diameter), these specimens are highly scattering. As expected, selecting a slit width of 3.25 μm (twice the approximate diameter of our excitation beam) improved contrast and reduced background, particularly in the direction of beam-scanning. There was an optimal range of slit widths, because slits greater than 3.25 μm exhibited more scattered light, whereas slit widths less than our beam diameter removed in-focus signal (data not shown). Even though some scattered light is still present after slit-scanning due to our relatively large slit width, the slit reduced background at the periphery of the pollen grain and improved contrast between the pollen periphery and interior. (See line profiles in Fig. 6a; note that slit-scanning curves are steeper at the edges of the pollen, and fall to a lower value at the center due to the reduction in background.) Extraneous scattered light is not effectively modeled by our deconvolution algorithm, so we expected that any reduction in scattering due to slit-scanning would also improve deconvolved images. Indeed, the improvements offered by slit-scanning were observed with deconvolved images of pollen (Fig. 6a) and when imaging specimens such as GFP-histone-labeled nuclei in live embryos of *Caenorhabditis elegans* (compare left and right columns in Fig. 6b, and see supplementary video 5 (http://www.biolbull.org/content/supplemental) all deconvolved. To quantify improvements as a result of the slit, we measured the signal-to-background ratio (SBR) between nuclei and the background in Figure 6b. The SBR was two to three times better with the slit, confirming the greater background rejection afforded by slit-scanning. These improvements were observed whether we imaged these samples in stage-scanning or conventional diSPIM mode (data not shown). We conclude that synchronized slit-scanning with a rolling shutter improves contrast and sectioning in diSPIM for both live and fixed samples.

As a final demonstration of combined slit- and stage-scanning modalities, we applied these to visualize developing neurons in nematode embryos (Kumar *et al.*, 2015). These samples are challenging to image because they are sensitive to photobleaching and/or photodamage (and thus benefit from diSPIM). In addition, developing neurites represent fine, diffraction-limited structures, which are easier to resolve with a thin sheet, *i.e.*, with stage-scanning; and the embryo causes increasing scattering, particularly at late stages once the cuticle forms (so that imaging benefits from slit-scanning). We imaged an embryo coexpressing a *Pncs-1::membrane-tether(PH)::GFP* reporter construct, which labeled developing neurons, and nuclear-localized mCherry, a fluorophore tracer, every minute from the two-cell stage into the three-fold stage. Green fluorescent protein (GFP) expression in neurons became apparent around the bean stage (Fig. 4a), and expression progressively increased throughout development (Fig. 4b–d). Fine neuronal structure was apparent at both early (Fig. 4b) and late time points in development (Fig. 4c, d). At early time points, we observed neurite outgrowth (Fig. 4b). As embryos reached the three-fold stage, most neurite outgrowth events appeared to have concluded (Fig. 4c). However, we observed *Pncs-1::membrane-tether(PH)::GFP* expression in a new set of neurons, with fine structure visible at neurite tips in these cells (Fig. 4d). Based on their position and morphology, we identified these structures as the ciliated endings of amphid neuron dendrites. Concurrent imaging of the mCherry channel (Fig. 4e–h) allowed for assignment of the embryo to specific developmental stages.

Discussion

While stage- and slit-scanning are fully compatible with existing dual-view inverted selective plane illumination microscopy (diSPIM) systems, they are not applicable to all samples. For stage-scanning applications, the sample must adhere to the coverslip; loosely attached samples will move relative to the stage during scanning, causing motion artifacts and image degradation. For such samples, the slit-scanning method still may prove useful in removing out-of-focus light, when combined with conventional diSPIM. We also note that slit-scanning—at least as implemented here—requires careful synchronization of rolling shutter and sweep of the light sheet; slit-width selection depends on both exposure time and readout time (see Materials and Methods). Acquisition time and signal-to-noise and signal-to-background ratios are thus tightly coupled. For many thin, transparent, or dim samples (*e.g.*, fluorescent labels in tissue culture cells, such as the mitochondria in Fig. 3), the slit-scanning feature is likely to be of limited benefit; images with an acceptable signal-to-background ratio (SBR) and better signal-to-noise ratio can be obtained more simply by operating the camera "conventionally." Conversely, for more scattering samples slit-scanning offers obvious improvements in SBR (Fig. 6). Thus, we anticipate that, for many samples, combined slit- and stage-scanning will offer better imaging than conventional diSPIM. We are excited about applying these techniques in concert with new methods for untwisting (Christensen *et al.*, 2015) and displaying (Santella *et al.*, 2015) 4D embryonic data, which will aid in the construction of a 4D neurodevelopmental atlas in *Caenorhabditis elegans* (Santella *et al.*, 2015).

In our experience, motorized stages such as the one we used are incapable of precise (sub-micron) steps at high speeds ($<$ 10 ms). For this reason, we operated the stage at constant velocity during stage-scanning. A future improvement of the system may be to replace the motorized mechanical stage with a more sensitive and precise piezoelectric stage. This would eliminate the need to accelerate

and/or decelerate the stage (Fig. 2c), shortening acquisition time and allowing a more precise match between stage position and camera exposure.

Acknowledgments

We thank Jim Sims, Patrick Gregorio, and Shelley Brankner (Hamamatsu Corporation) for help in integrating the sCMOS slit-scanning function with our LabVIEW program; Jon Daniels and Gary Rondeau (Applied Scientific Instrumentation) for useful discussions on stage-scanning; William Mohler (University of Connecticut Health Center) for encouragement; William Gandler (NIH Center for Information Technology) for help with MIPAV; Nicole Tashakkori and John Joseph for acquiring embryo data used for lineaging; and Hank Eden and Talley Lambert for their comments on the manuscript. We also thank the Research Center for Minority Institutions program and the Institute of Neurobiology at the University of Puerto Rico for providing a meeting and brainstorming platform. MG acknowledges funding from the National Natural Science Foundation of China (grants no. 61427807, 61271083, and 61525106); Shenzhen Innovation Funding (grants no. SGLH20131010110119871 and GJHZ20140415152115754); and Zhejiang Province Science and Technology Projects (grant no. 2015C33061). Much of this work was conducted at the Marine Biological Laboratory at Woods Hole, either through the Whitman Program (DAC-R and HS) or a Grass Foundation Fellowship (to AK). Support for this work was provided by the Intramural Research Programs of the National Institute of Biomedical Imaging and Bioengineering, and by NIH grants no. U01 HD075602 and R24OD016474.

Literature Cited

Ahrens, M. B., M. B. Orger, D. N. Robson, J. M. Li, and P. J. Keller. 2013. Whole-brain functional imaging at celluler resolution using light-sheet microscopy. *Nat. Methods* **10:** 413-420.

Bao, Z., J. I. Murray, T. Boyle, S. L. Ooi, M. J. Sandel, and R. H. Waterson. 2006. Automated cell lineage tracing in *Caenorhabditis elegans. Proc. Natl. Acad. Sci. USA* **103:** 2707-2712.

Baumgart, E., and U. Kubitscheck. 2012. Scanned light sheet microscopy with confocal slit detection. *Opt. Express* **20:** 21805-21814.

Chhetri, R. K., F. Amat, Y. Wan, B. Höckendorf, W. C. Lemon, and P. J. Keller. 2015. Whole-animal functional and developmental imaging with isotropic spatial resolution. *Nat. Methods* **12:** 1171-1178.

Christensen, R. 2015. diSPIM image processing using MIPAV (Medical Image Processing, Analysis, and Visualization). [Online]. diSPIM Wiki. Available: http://dispim.org/software/mipav_generatefusion [2015, December 5].

Christensen, R. P., A. Bokinsky, A. Santella, Y. Wu, J. Marquina-Solis, M. Guo, I. Kovacevic, A. Kumar, P. W. Winter, N. Tashakkori *et al.* 2015. Untwisting the *Caenorhabditis elegans* embryo. *eLife* **4:** e10070.

de Medeiros, G., N. Norlin, S. Gunther, M. Albert, L. Panavaite, U.-M. Fiuza, F. Peri, T. Hiiragi, U. Krzic, and L. Hufnagel. 2015. Confocal multiview light-sheet microscopy. *Nat. Commun.* **6:** 8881-8889.

Dean, K. M., P. Roudot, E. S. Welf, G. Danuser, and R. Fiolka. 2015. Deconvolution-free subcellular imaging with axially swept light sheet microscopy. *Biophys. J.* **108:** 2807-2815.

Fischer, R. S., Y. Wu, P. Kanchanawong, H. Shroff, and C. M. Waterman. 2011. Microscopy in 3D: a biologist's toolbox. *Trends Cell Biol.* **21:** 682-691.

Giurumescu, C. A., S. Kang, T. A. Planchon, E. Betzig, J. Bloomekatz, D. Yelon, P. Cosman, and A. D. Chisholm. 2012. Quantitative semi-automated analysis of morphogenesis with single-cell resolution in complex embryos. *Development* **139:** 4271-4279.

Guo, M., and H. Shroff. 2015. Fiji plug-in for stage scan image reconstruction and tutorial. [Online]. diSPIM Wiki. Available: http://dispim.org/software/imagej_macro [2015, December 5].

Huisken, J., and D. Y. R. Stainier. 2009. Selective plane illumination microscopy techniques in developmental biology. *Development* **136:** 1963-1975.

Huisken, J., J. Swoger, F. Del Bene, J. Wittbrodt, and E. H. K. Stelzer. 2004. Optical sectioning deep inside live embryos by selective plane illumination microscopy. *Science* **305:** 1007-1009.

Keller, P. J., A. D. Schmidt, J. Wittbrodt, and E. H. K. Stelzer. 2008. Reconstruction of zebrafish early embryonic development by scanned light sheet microscopy. *Science* **322:** 1065-1069.

Keller, P. J., A. D. Schmidt, A. Santella, K. Khairy, Z. Bao, J. Wittbrodt, and E. H. K. Stelzer. 2010. Fast, high-contrast imaging of animal development with scanned light sheet-based structured-illumination microscopy. *Nat. Methods* **7:** 637-642.

Kumar, A., and H. Shroff. 2015. diSPIM Image acquisition using LabVIEW. [Online]. diSPIM Wiki. Available: http://dispim.org/software/labview [2015, December 5].

Kumar, A., Y. Wu, R. Christensen, P. Chandris, W. Gandler, E. McCreedy, A. Bokinsky, D. A. Colón-Ramos, Z. Bao, M. McAuliffe *et al.* 2014. Dual-view plane illumination microscopy for rapid and spatially isotropic imaging. *Nat. Protocols* **9:** 2555-2573.

Kumar, A., D. A. Colón-Ramos, and H. Shroff. 2015. Watching a roundworm develop with a sheet of light. *Physics Today* **68:** 58-59.

McAuliffe, M. J., F. M. Lalonde, D. McGarry, W. Gandler, K. Csaky, and B. L. Trus. 2001. Medical image processing, analysis and visualization in clinical research. Pp. 381-386 in *Proceedings, 14th IEEE Symposium on Computer-Based Medical Systems,* 381; *CBMS 2001.* IEEE Computer Society, Los Alamitos, CA.

Mickoleit, M., B. Schmid, M. Weber, F. O. Fahrbach, S. Hombach, S. Reischauer, and J. Huisken. 2014. High-resolution reconstruction of the beating zebrafish heart. *Nat. Methods* **11:** 919-922.

Perry, S. W., J. P. Norman, J. Barbieri, E. B. Brown, and H. A. Gelbard. 2011. Mitochondrial membrane potential probes and the proton gradient: a practical usage guide. *BioTechniques* **50:** 98-115.

Planchon, T. A., L. Gao, D. E. Milkie, M. W. Davidson, J. A. Galbraith, C. G. Galbraith, and E. Betzig. 2011. Rapid three-dimensional isotropic imaging of living cells using Bessel beam plane illumination. *Nat. Methods* **8:** 417-423.

Presley, A. D., K. M. Fuller, and E. A. Arriaga. 2003. MitoTracker Green labeling of mitochondrial proteins and their subsequent analysis by capillary electrophoresis with laser-induced fluorescence detection. *J. Chromatogr. B Anal. Technol. Biomed. Life Sci.* **793:** 141-150.

Santella, A., Z. Du, S. Nowotschin, A.-K. Hadjantonakis, and Z. Bao. 2010. A hybrid blob-slice model for accurate and efficient detection of fluorescence labeled nuclei in 3D. *BMC Bioinformatics* **11:** 580-593.

Santella, A., R. Catena, I. Kovacevic, P. Shah, Z. Yu, J. Marquina-Solis, A. Kumar, Y. Wu, J. Schaff, D. A. Colón-Ramos *et al.* 2015. WormGUIDES: an interactive single cell developmental atlas and tool for collaborative multi-dimensional data exploration. *BMC Bioinformatics* **16:** 189.

Santi, P. A., S. B. Johnson, M. Hillenbrand, P. Z. GrandPre, T. J.

Glass, and J. R. Leger. 2009. Thin-sheet laser imaging microscopy for optical sectioning of thick tissues. *BioTechniques* **46:** 287-294.

Schneider, C. A., W. S. Rasband, and K. W. Eliceiri. 2012. NIH Image to ImageJ: 25 years of image analysis. *Nat. Methods* **9:** 671-675.

Silvestri, L., A. Bria, L. Sacconi, G. Iannello, and F. S. Pavone. 2012. Confocal light sheet microscopy: micron-scale neuroanatomy of the entire mouse brain. *Opt. Express* **20:** 20582-20598.

Stelzer, E. H. K. 2015. Light-sheet fluorescence microscopy for quantitative biology. *Nat. Methods* **12:** 23-26.

Sulston, J. E., E. Schierenberg, J. G. White, and J. N. Thomson. 1983. The embryonic cell lineage of the nematode *Caenorhabditis elegans. Dev. Biol.* **100:** 64-119.

Twig, G., A. Elorza, A. J. A. Molina, H. Mohamed, J. D. Wikstrom, G. Walzer, L. Stiles, S. E. Haigh, S. Katz, G. Las *et al*. 2008. Fission and selective fusion govern mitochondrial segregation and elimination by autophagy. *EMBO J.* **27:** 433-446.

Winter, P. W., and H. Shroff. 2014. Faster fluorescence microscopy: advances in high speed biological imaging. *Curr. Opin. Chem. Biol.* **20:** 46-53.

Wu, Y., A. Ghitani, R. Christensen, A. Santella, Z. Du, G. Rondeau, Z. Bao, D. A. Colón-Ramos, and H. Shroff. 2011. Inverted selective plane illumination microscopy (*i*SPIM) enables coupled cell identity lineaging and neurodevelopmental imaging in *Caenorhabditis elegans*. *Proc. Natl. Acad. Sci. USA* **108:** 17708-17713.

Wu, Y., P. Wawrzusin, J. Senseney, R. S. Fischer, R. Christensen, A. Santella, A. G. York, P. W. Winter, C. M. Waterman, Z. Bao *et al*. 2013. Spatially isotropic four-dimensional imaging with dual-view plane illumination microscopy. *Nat. Biotechnol.* **31:** 1032-1038.